

TWO VIEWING THEORY ON ATMOSPHERE CORRECTION IN OCEAN COLOR ALGORITHM

SISIR KUMAR DASH¹, TASUKU TANAKA², AND RYUTARO TATEISHI³

Abstract

A new algorithm for retrieving optical thickness and surface reflectance, data in the visible bands from satellites is developed. The proposed algorithm is to solve the simultaneous equation of two unknown variables, i.e. aerosol optical thickness (To) and surface reflectance (r). In term of difference from the conventional and, one directional retrieval algorithm, we do not need the spectral characteristics of aerosol. We solve the equation by forward calculation using the 6S transfer code. The two observational equations change linearly within the domain where we solve the solution. We estimate the chlorophyll-a concentration from the evaluated r. This method is validated against Global Imager (GLI) data, which has two independent data for one pixel in both tilting and nadir viewing.

Keywords : GLI, 6S, Radiative Transfer, Reflectance, Rayleigh, Mie.

I. Introduction

The ocean chlorophyll concentration retrieved from satellite observation data consists of the two main processes: atmospheric correction and in-underwater algorithm (Martin, 2004). In this paper, we introduce a new method for atmospheric correction. The purpose of atmospheric correction is to extract the water-leaving radiance from observed radiance scattered in the several visible bands. The observed radiance is contained with radiance, divided into two parts: the Rayleigh or molecular scattering, and the Mie or aerosol scattering. The type of scattering process depends on the size of molecules or particles relative to the incident wavelength (A.). The Rayleigh scattering dominates in molecular and its characteristic does not vary with time and space in the visible regions, while the Mie scattering varies temporally and spatially and depends on the aerosol. The sensor-

measured radiance at the top of the atmosphere (TOA) can be written by $L_i(\lambda)$ for each pixel, which is converted to the general reflectance $\rho_i(\lambda)$ by the following equation

$$\rho_i(\lambda) = \frac{\pi L_i(\lambda)}{F_0(\lambda) \cos \theta_s} \dots\dots\dots(1)$$

where $F_0(A_s)$ is the extraterrestrial solar irradiance and Q_s is the solar zenith angle for that pixel. Neglecting the influence of direct sun glitter and contribution of whitecaps at sea surface, the total general reflectance at the TOA, $\rho_t(A_s)$ is described as (Gordon et al, 1997)

$$\rho_t(\lambda) = \rho_r(\lambda) + \rho_a(\lambda) + \rho_{ra}(\lambda) + t(\lambda) \rho_w(\lambda) \dots\dots\dots(2)$$

1. Graduate School of Science & Technology, Chiba University, 1-33, Yayoi-Cho, Inage-Ku, Chiba-shi, Japan.
 2. Department of Mechanical Engineering, Yamaguchi University, Japan.
 3. Centre for Environmental Remote Sensing, Chiba University, 1-33, Yayoi-cho, Inage-Ku, Chiba-shi, 261-0001, Japan

where $\tau(\lambda)$ is the diffuse transmittance of the atmosphere. $p_r(X)$, $p_{ra}(X)$, $p_{ra}(X)$ are the scattered radiances that are contributed from Rayleigh, aerosol and interaction effect between air molecules and aerosol respectively. $p_w(\lambda)$ is a equivalent reflectance from water-leaving radiance.

The basic aim is to retrieve $p_w(\lambda)$ from $p_r(\lambda)$. The observed $p_r(X)$ contains with a function of two unknown variables $p_w(X)$ and aerosol optical thickness (τ), $p_a(\lambda)$ and $p_{ra}(X)$ are functions of x_a . In the conventional ocean color algorithms (Kahru and Mitchell, 1999; Fukushima *et al.*, 2003), $p_w(\lambda)$ is assumed as zero in the

near infrared band, so as to get x_a using Eq. (2). Extrapolating x_a from near infrared to visible band, and substituting the extrapolated x_a into the Eq. (2), $p_w(\lambda)$ can be calculated. Applying $p_w(\lambda)$ in the several visible bands into a in-water algorithm (Gordon and Wang, 1994), chlorophyll concentration can be estimated. Wide spectral application of x_a is critical to determine $P_w(\lambda)$ in this spectral method, because X_a is also function of wide spectral characteristic. The geometry of the radiative transfer process is shown in Fig. 1. The direction of input solar radiance i_0 , the directions of

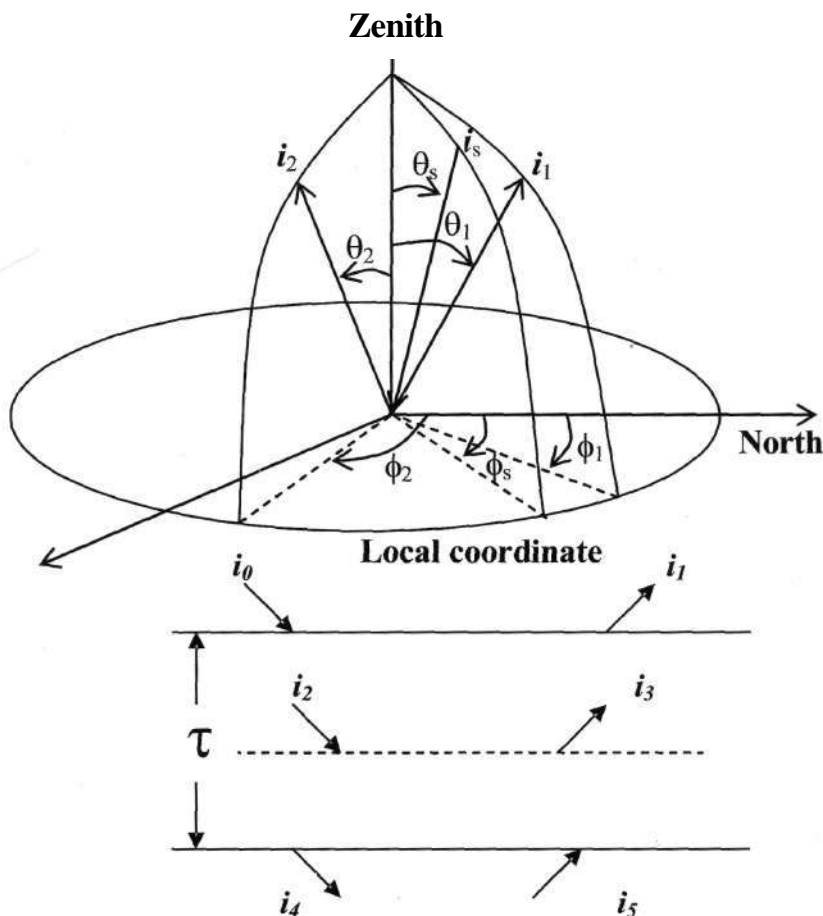


Figure 1. Geometry of the radiative transfer

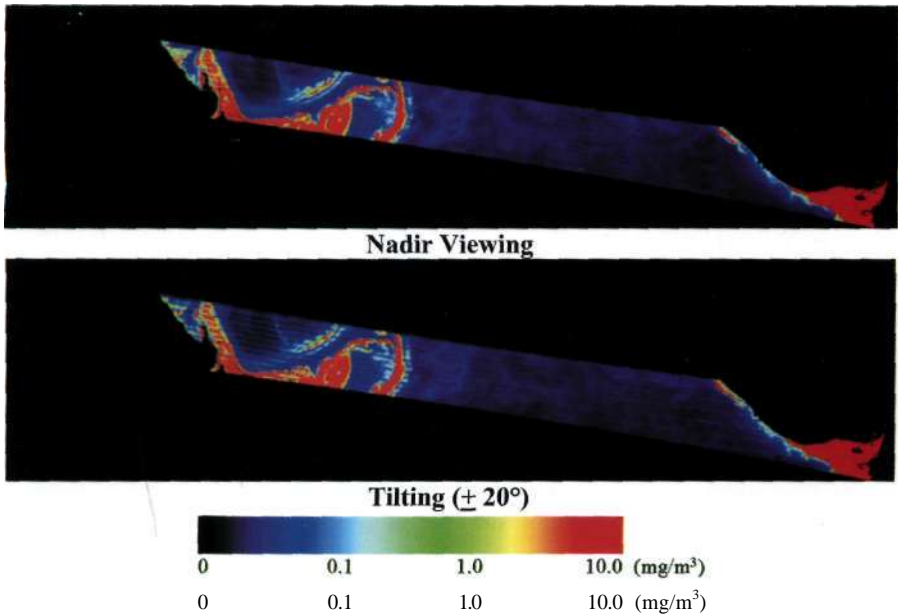


Figure 2. GLI Chlorophyll-a (mg/m³) concentration in two viewing directions (Date: 03 October 2003)

satellite observation are shown in two different viewing directions looking the same pixel as i_1 and i_2 . We employ the polar coordinate system in which the zenith angle (θ) is measured from the zenith and the azimuth angle (ϕ) is measured from the north of the local horizontal plane. We denote the cosine of the zenith angle in the direction i_n as μ_n .

GLI is an instrument aboard ADEOS-II which has a tilting mechanism to avoid sun glitter. The mechanism also yields two directional observations for one pixel in the

limited overlap zone. In Level 2, GLI standard product is provided by the JAXA archive, we can obtain $p_w(A_-)$ from normalized water leaving radiance (nL_w), using Eq. (2). Theoretically, the values of $p_w(A_-)$ for nadir and tilt viewing should be identical, but in practice, there are different values, which are shown in Table 1. We can also observe Level 2 different chlorophyll products, which is shown in Fig. 2. Therefore, we try to develop a new atmospheric correction method, named Two Directional Method with no relation

Table 1. Comparison of $p_w(443nm)$ and Chlorophyll Concentration using Level - 2 Data Sets for the Two Observing Directions.

Pixel No.	D1		D2	
	$p_w(443nm)$	Chlorophyll concentrations (mg/m3)	$p_w(443nm)$	Chlorophyll concentrations (mg/m3)
1	0.013	2.4345	0.015	2.979
81	0.040	0.408	0.045	1.1085
161	0.035	0.3705	0.043	0.5775
241	0.035	2.928	0.020	3.918
321	0.034	0.3555	0.042	0.5925
401	0.022	3.408	0.023	3.7425

to spectral determination. We can obtain x_a in visible bands from the numerical simulation code (6S). We discuss about the GLI data and 6S code in Section. 2. Radiative transfer process is discussed in Section. 3. Solution for r and x_a are discussed in Section 4.

II. GLI Data and 6S code

a. Sensor characteristics

GLI is an optical sensor aboard ADEOS-II, observing in global scale and measuring the physical content such as chlorophyll, dissolved organic substance, surface temperature, vegetation distribution, vegetation biomass, distribution of snow and ice, and albedo of snow and ice, etc. It has 23 bands in visible and near-infrared region (VNIR), 6 bands in short-wave length infrared region (SWIR), and 7 bands in middle and thermal infrared region for its multispectral observation. The swath width is 1600km by a mechanical scanning in the cross-track direction. GLI has a tilting mechanism to avoid the sun glitter.

b. GLI Imagery from the North Indian Ocean

We use two sets of GLI Images, acquired on 3 October 2003 along north Indian Ocean. The false color composite image (D1: nadir viewing and D2: + 20° tilting) are shown in Fig. 3. The

overlapping areas from D1 to D2 contains a narrow stripe where each pixel is observed in two directions. The geometrical rearrangement is an integral part of processing where nadir viewing and tilting images are brought one to one correspondence. Two pixels were selected in the high and low concentration of chlorophyll as Pixel-1 and Pixel-81 respectively, which are described in later parts in this paper.

c. 6S code

Second Simulation of the Satellite Signal in the Solar Spectrum (6S) is a computer code which can accurately simulate the radiative transfer process in the atmosphere with limited computing resources and a fast approximation (Vermote *et al*, 1997). The processing scheme is described in Fig. 4. The inputs to the 6S code are sun and satellite zenith and azimuth angles. Selection of the maritime aerosol models in the tropical regions are additional input to the above code. GLI wavelength and GLI altitude parameters are also incorporated. The 6S code calculates the p_r , with the inputs of r and x_a . Our problem is an inversion problem, or to evaluate r and x_a from two different p_r . We employ the 6S code as a method which yield the given p_r by trial and error method. In the process of the 6S

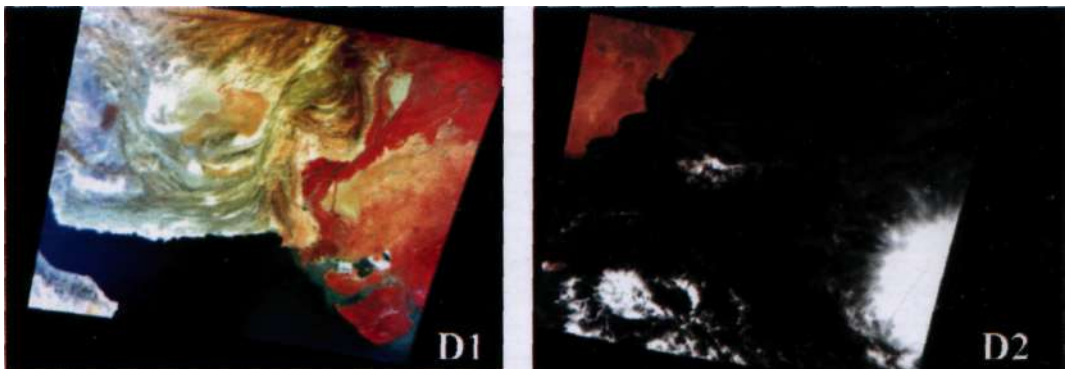


Figure 3. False Color composite of GLI (R: B14, G: B8, B: B5)

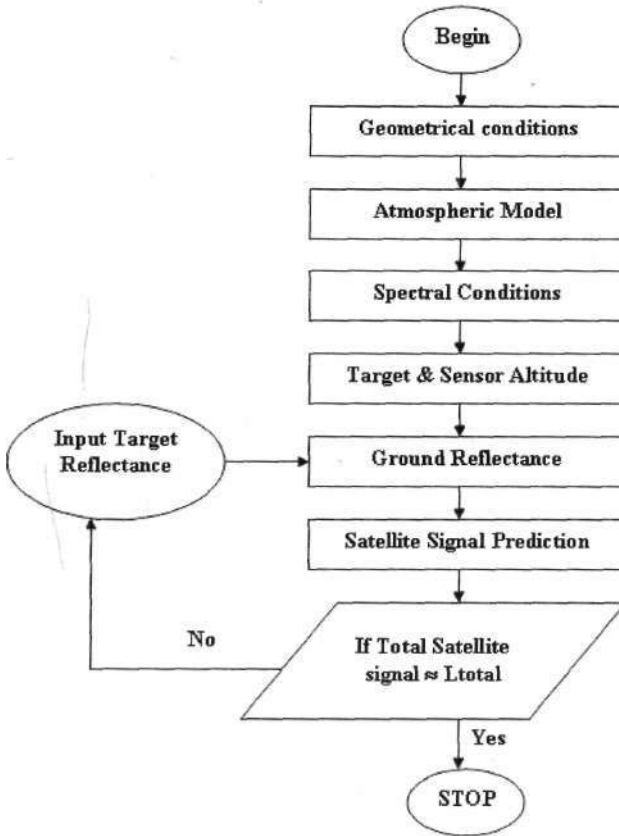


Figure 4. Flow chart showing the schematic procedure of 6S code

simulation, the input target reflectance (r) evaluates the general reflectance (ρ_t) with an error of + 0.00001 [reflectance unit].

III. Radiative Transfer

a. Scattering function

For a finite optical thickness with incident radiance from the upper surfaces, the radiances emerging from the upper surface (u) $I(0, i_1)$ can be expressed by the scattering function $S(\tau, i_1, i_s)$ as Eq. 4 below

$$I(0, i_1) = \int_0^{\tau} \frac{1}{4 \cos^2 \theta_1} \int_u S(\tau, i_1, i_s) I(0, i_s) d\tau_s \dots \dots \dots (4)$$

$$I(\tau, i_2) = \int_0^{\tau} \frac{1}{4 \cos^2 \theta_2} \int_l T(\tau, i_2, i_s) I(0, i_s) d\tau_s \int \exp\left[-\int_{\tau}^{\tau'} \frac{1}{\cos \theta_2}\right] I(0, i_2) \dots \dots \dots (5)$$

$$I(0, i_0) = F_0 \int_{i_0} i_s \dots \dots \dots (6)$$

Chandrasekhar, 1960).

Similarly, the radiance emerging from the lower surface (l) $I(\tau, i_2)$ can be expressed by the transmittance function $T(\tau, i_2, i_s)$ as Eq. 5.

In the satellite remote sensing, the incident radiance is the solar irradiance only and is expressed as, Eq. 6

$$I(0, i_1) = \frac{S(\tau, i_1, i_s)}{4\pi \cos\theta_1} F_0 \dots\dots\dots (7)$$

$$I(\tau, i_2) = \frac{T(\tau, i_2, i_s)}{4\pi \cos\theta_2} F_0 \dots\dots\dots (8)$$

$$\lim_{\tau \rightarrow 0} S(\tau, i_n, i_s) = \lim_{\tau \rightarrow 0} T(\tau, i_n, i_s) = \tau P(i_n, i_s) \dots\dots\dots (9)$$

Where δ is the Dirac delta function, F_0 is the solar irradiance and S is the direction of the sun. Thus, we obtain $I(0, z'i)$ and $I(xj2)as$ shown in Eq. 7 and Eq. 8 respectively.

For the thin optical thickness, we have the single approximation as Eq. 9.

b. Surface Reflection

On a Lambertian surface, the incident radiance $I(i_2)$ is applied in the direction of ii . The reflected radiance $I(p)$ in the direction of h is expressed in Eq. 10 below.

Here r is the surface reflectance. As the reflected radiance from the lower surface is independent of the direction due to Lambertian surface, we designate it I_g . The generalized reflectance $p(z, h, i_s)$ observed by satellites (Chandrasekhar, 1960) is given in Eq. 11 below.

where $t(i)$ and s are the transmittance functions described in the Appendix.

For $x, r \ll 1$, the first order approximation in r in the second term in Eq. 11 becomes r . Now the first order approximation of Eq. 11 is written as Eq. 12 (Tanaka and Wang, 2004)

This approximation is called as the single scattering approximation that has been applied to many analyses. But the single approximation is not enough to retrieve r . We found that the first order expansion of the scattering function (s) is sufficient, while the second order expansion in Eq. 12 is necessary.

In Eq. (11) the optical thickness is the combination one of the Rayleigh and Mie scattering. Because of the property of addition of optical thickness, we decompose the combined optical thickness and the scattering phase function for the Rayleigh and Mie scatterings as Eq. 13.

$$I(i_3) = \frac{r}{\pi} \int I(i_2) \mu_2 d\Omega_2 = I_g(\tau) \dots\dots\dots (10)$$

$$\rho_r(\tau, i_1, i_s) = \frac{S(\tau, i_1, i_s)}{4\mu_1 \mu_s} + \frac{r}{1-r\bar{s}} \left[\frac{t(\mu_s)}{\mu_s} + \exp\left(-\frac{\tau}{\mu_s}\right) \right] \left[\frac{t(\mu_1)}{\mu_1} + \exp\left(-\frac{\tau}{\mu_1}\right) \right] \dots\dots (11)$$

$$\rho_r(\tau, i_1, i_s) = \frac{\tau P(\tau, i_1, i_s)}{4\mu_1 \mu_s} + r \dots\dots\dots (12)$$

$$\tau = \tau_r + \tau_a \text{ and } \tau P(\cos \Theta) = \tau_r P_r(\cos \Theta) + \tau_a P_a(\cos \Theta) \dots\dots\dots (13)$$

$$\rho_r(\tau_a, r) = \frac{S(\tau_r + \tau_a)}{4\mu_1\mu_s} + \frac{r}{1-r\bar{s}} \left[\frac{t(\tau_r + \tau_a, \mu_s)}{\mu_s} + \dots \right] \dots \dots \dots$$

$$\exp\left(-\frac{\tau_r + \tau_a}{\mu_s}\right) \left[\frac{t(\tau_r + \tau_a, \mu_1)}{\mu_1} + \exp\left(-\frac{\tau_r + \tau_a}{\mu_1}\right) \right] \dots \dots \dots (14)$$

Substituting Eq. 13 into Eq. 11 we obtain the observation equation as Eq. 14:

IV. Results and Discussions

a. Solution for r and x_a in the simultaneous equations

We have two unknown variables r and X_a in the observation equation. From the simultaneous equation, we solve both r and X_a . The scheme is as follows:

(1) We assume X_a is zero. The observing equation can be well approximated by the equation below (Eq. 15).

where $f(\cos \theta)$ is the phase function of Rayleigh scattering and is given as Eq. 16 below.

here θ is the scattering angle (see the Appendix). The Rayleigh optical thickness (τ_r) is given in Table 2 and the observed generalized reflectance (ρ_r) is given in Table 3. From the observing Eq. (15), we solve n for nadir viewing pixel. We obtain n in the same manner for tilt viewing pixel. The result of n and r are not equal except for $\theta = 0$.

(2) Increasing θ , we evaluate ρ_r by the 6S code up to fifth decimal value. Of course, the resulted ρ_r differs from the

satellite observed values. Then, fixing ρ_r , we try to find r which yields the observed ρ_r with an error of + 0.00001 [Reflectance unit]. We designate the results of n that satisfies the observed reflectance ρ_r . In the similar manner, we obtain r . If m equals to n , we attain the solution.

(3) Repeating the above procedure we attain the solution that $r/n = n/r = r$.

For all purposes, the exact expression of Eq. (15) is not expressed in an explicit form but we can obtain it implicitly by the 6S code.

We have solutions for six bands (443, 460, 490, 520, 545 and 565 nm) for six pixels. Results from pixel-1 and pixel-81 show in the Fig. 5 and Fig. 6 respectively. In all the cases, the relation between X_a and r shows linear and it intersects each others for D1 and D2 scenes. The slope and intercepts for both D1 and D2 were calculated. The estimated X_a and r are shown in Table 4. Applying r into the band ratio ocean color in-water algorithm (Kahru and Mitchell, 1999; Fukushima et al, 2003), we obtain the chlorophyll concentration shown in Table 5. Due to uncertainty, negative X_a is not considered for chlorophyll estimation.

$$\rho_r(\tau_r, \theta, i_s) = \frac{\tau_r P(\cos \theta)}{4\mu_1\mu_s} + n - \frac{n\tau_r}{2\mu_s} - \frac{n\tau_r}{2\mu_1} \dots \dots \dots (15)$$

$$P(\cos \theta) = \frac{3}{4} (1 + \cos^2 \theta) \dots \dots \dots (16)$$

Table 2. Rayleigh optical thickness showing for GLI bands (1-19)

Band Number	Central wavelength (nm)	Rayleigh Optical Thickness
1	380	0.44861
2	400	0.36092
3	412	0.31927
4	443	0.23887
5	460	0.20378
6	490	0.15699
7	520	0.12312
8	545	0.10165
9	565	0.08778
10	625	0.05823
11	666	0.04527
12	678	0.04199
13	680	0.04137
14	710	0.03474
15	710	0.03474
16	749	0.02784
17	763	0.02587
18	865	0.01565
19	865	0.01565

Table 3 Generalised Reflectance (1) for six bands in D1 and D2

Wavelength (nm)	Viewing	Pixel-1	Pixel-81
443	D1	0.138649	0.136116
	D2	0.152415	0.152036
460	D1	0.126284	0.124553
	D2	0.139919	0.138368
490	D1	0.108381	0.107156
	D2	0.119284	0.120555
520	D1	0.092834	0.088368
	D2	0.103061	0.099988
545	D1	0.081668	0.077175
	D2	0.091107	0.088823
565	D1	0.071033	0.064170
	D2	0.078318	0.073721

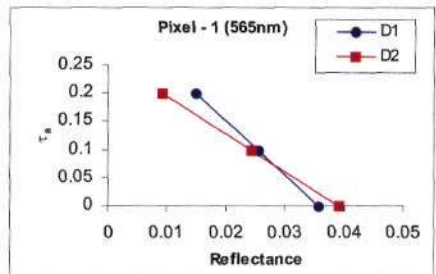
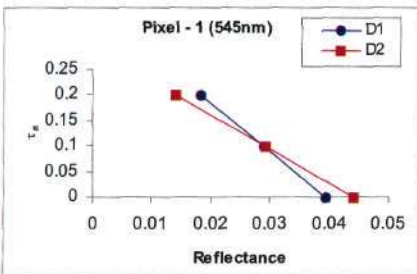
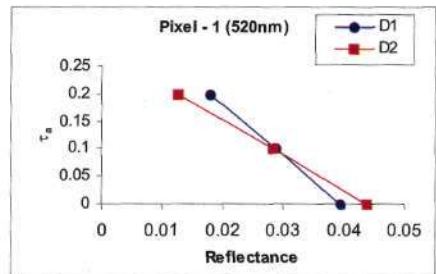
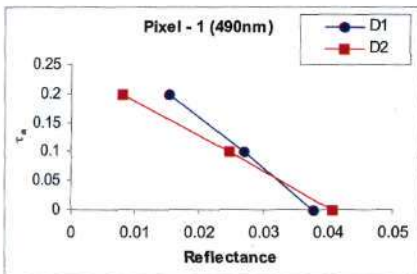
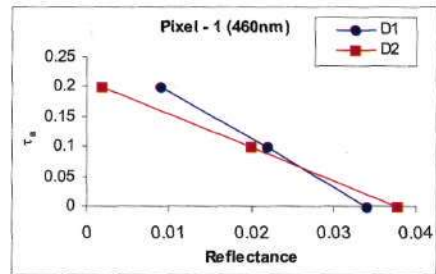
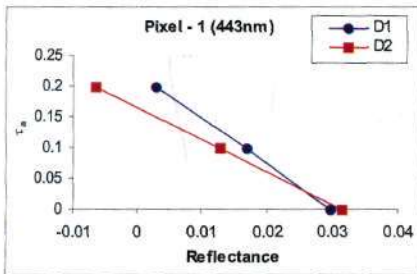
Table 4. Estimated T_a and r showing along with wavelength for all six pixels

Pixel No	L		81		161		241		321		401	
	r	T_a	r	T_a								
443	0.0257	0.0310	0.0238	0.0653	0.0259	0.0508	0.0244	0.0311	0.0288	0.0028	0.0324	-0.0368
460	0.0257	0.0670	0.0299	0.0557	0.0312	0.0428	0.0297	0.0180	0.0340	-0.0164	0.0368	-0.0523
490	0.0314	0.0579	0.0301	0.0914	0.0325	0.0638	0.0299	0.0542	0.0320	0.0344	0.0347	0.0068
520	0.0297	0.0900	0.0271	0.0927	0.0283	0.0749	0.0312	0.0682	0.0289	0.0355	0.0415	-0.0287
545	0.0283	0.1055	0.0240	0.1196	0.0258	0.0951	0.0288	0.0955	0.0272	0.0497	0.0393	-0.0016
565	0.0281	0.0736	0.0196	0.0969	0.0205	0.0850	0.0312	0.0563	0.0218	0.0476	0.0464	-0.1231

/

Table 5. Chlorophyll (mg/m^3) values shown using GLI Level-2 data and Estimated chlorophyll

Pixel No	Chl-a(D1)	Chl-a (D2)	Estimated Chlorophyll
1	2.4345	2.979	3.187
81	0.408	1.1085	0.946
161	0.3705	0.5775	0.582
241	2.928	3.918	3.861
321	0.3555	0.5925	0.574
401	3.408	3.7425	NA

Figure 5. Relationship between x_a and Reflectance in different wavelength in the visible region (High concentration of chlorophyll regions)

b. Error estimation

The vicarious calibration coefficient of GLI bands in the visible regions seems to be too low (Yoshida et al, 2005), and is affected severely on x_a and r . Typically,

in clear water the contribution of water leaving radiance to TO A radiance is ~10% in the blue (A, ~440nm), 5% in the green (A, ~550nm), and negligible in the near-infrared ($X > 750\text{nm}$). The 5% error of

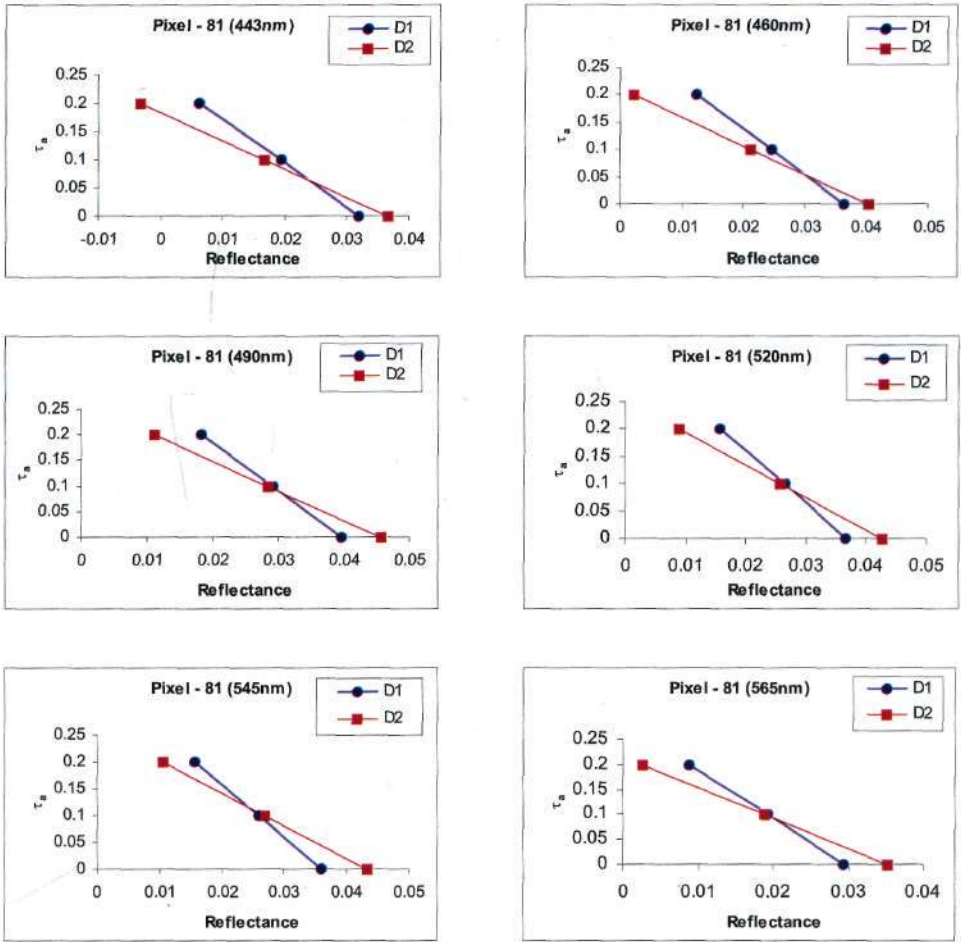


Figure 6. Relationship between x_a and Reflectance in different wavelength in the visible region (Low concentration of chlorophyll regions)

water leaving radiance causes only a maximal error of 0.5% on the TOA radiance. We estimated the error for both X_a and r in blue (443nm) and green (545nm) bands of GLI and their error bars (Fig. 7). The estimated error for T_{∞} is large amount, compared to error involved in r . The 15% error in r is considered as the maximum error contributed for further estimation of chlorophyll-a concentration.

Conclusion

We have evaluated the chlorophyll concentration in certain areas in the GLI nadir and the tilt looking data by the Two

Direction Method. The chlorophyll concentrations that obtained are higher than those by the conventional method. We also evaluate the Rayleigh scattering by the approximation given in Eq. (15) and the results agree very well with those evaluated by the 6S code. For the cases $x_{a550} \neq 0$, we evaluate r by trial and error method using the 6S code. The slopes of the iso-general reflectance p are linear. This suggests that we can evaluate the solution by a linear approximation not by the 6S code.

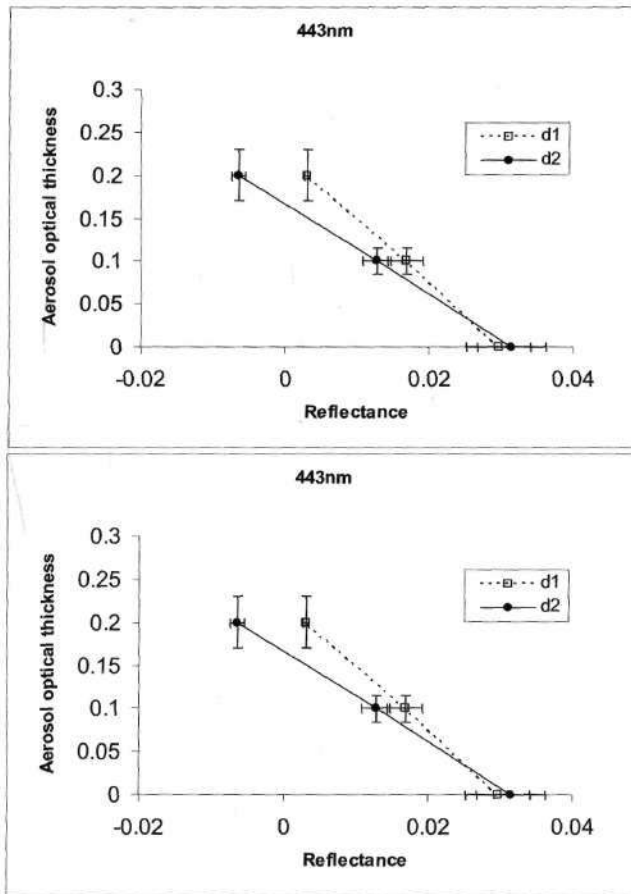


Figure 7. Error % of x_a and Reflectance at 443nm and 545nm

Acknowledgement

This research is a joint research project between Chiba University and Japan Aerospace Exploration Agency (JAXA). The author wishes to acknowledge Mr. Yashshi Mitomi, RESTEC, JAXA for providing GLI data and its processing scheme and Mr. Kenta Kosugi for his contributed work during his master degree.

References

- Chandrasekhar, S. 1960. Radiative Transfer. Dover Publications, New York.
- Fukushima, H., M. Toratani, A. Tanaka, W. Z. Chen, and H. Murakami. 2003. ADEOS-II/GLI ocean color atmospheric correction: early phase result. Proc. Of SPIE, 5155:91-99. ,

GLI Home Page:

<http://suzaku.eorcjaxa.jp/GLI/>

- Gordon, H. R. and M. Wang. 1994. Retrieval of water-leaving radiance and aerosol optical thickness over the oceans with SeaWiFS: A Preliminary algorithm. Applied Optics, 33(3):443-452.
- Gordon, H. R, T. Du, and T. Zhang. 1997. Remote sensing of ocean color and aerosol properties: resolving the issue of aerosol absorption. Applied Optics, 36(33):8670-8684.
- Kahru, M. and B. G. Mitchell. 1999. Empirical chlorophyll algorithm and preliminary SeaWiFS validation for California current. International Journal of Remote Sensing, 20(17):3423-3429.
- Martin, S. 2004. An Introduction to Ocean Remote Sensing. Cambridge Univ. Press.

Tanaka, T. and M. Wang. 2004. Solution of radiative transfer in anisotropic plane-parallel atmosphere. *Journal of Quantitative Spectroscopy & Radiative Transfer*, 83:555-577.

Yoshida, M., H. Murakami, Y. Mitomi, M. Hori, K. J. Thome, D. K. Clark and H. Fukushima. 2005. Vicarious calibration of GLI by ground observation data. *IEEE. Trans. Geosci. Remote Sensing*, 43(10):2167-2176.

Vermote, E., D. Tanre, J. L. Deuze, M. Herman, and J. J. Morcrette. 1997. Second Simulation of the satellite signal in the solar spectrum, 6S: An overview. *IEEE Trans. Geosci. Remote Sensing*, 35(3):675-686.

Appendix

The function $t(\mu_1)$ is calculated as shown below,

$$t(\mu_1) = \int_{2\pi:U} \frac{T(\tau, i_1, i_s)}{4\pi} d\Omega_s = \tau \int_{2\pi:U} \frac{P(i_1, i_s)}{4\pi} d\Omega_s \tag{17}$$

For combined optical thickness, substituting Eq. (13) we obtained

$$t(\mu_1) = \tau_r \int \frac{P_r(\cos \Theta)}{4\pi} d\Omega_3 + \tau_a \int \frac{P_a(\cos \Theta)}{4\pi} d\Omega_3 \tag{18}$$

Integrating Rayleigh Phase function

$$\begin{aligned} \tau_r \int \frac{P_r(\cos \Theta)}{4\pi} d\Omega_3 &= \tau_r \int \frac{3(1 + \cos^2 \Theta)}{4} \frac{d\Omega_3}{4\pi} = \tau_r \int \frac{3(1 + \cos^2 \Theta)}{4} \frac{d\phi_3 d\mu_3}{4\pi} \\ &= \int_0^1 \int_0^{2\pi} \frac{3(1 + \cos^2 \Theta)}{4} \frac{d\phi_3 d\mu_3}{4\pi} = \frac{\tau_r}{2} \end{aligned} \tag{19}$$

We calculate aerosol phase function implicitly by 6S code.

Scattering angle (Θ) is calculated as

$$\cos \Theta = \cos \theta_1 \cos \theta_s + \sin \theta_1 \sin \theta_s (\cos \phi_1 - \phi_s) \tag{20}$$